
This is an electronic reprint of the original article.
This reprint may differ from the original in pagination and typographic detail.

Viitanen, Ville; Sipilä, Tuomas; Sánchez-Caja, Antonio; Siikonen, Timo
CFD predictions of unsteady cavitation for a marine propeller in oblique inflow

Published in:
Ocean Engineering

DOI:
[10.1016/j.oceaneng.2022.112596](https://doi.org/10.1016/j.oceaneng.2022.112596)

Published: 15/12/2022

Document Version
Publisher's PDF, also known as Version of record

Published under the following license:
CC BY

Please cite the original version:
Viitanen, V., Sipilä, T., Sánchez-Caja, A., & Siikonen, T. (2022). CFD predictions of unsteady cavitation for a marine propeller in oblique inflow. *Ocean Engineering*, 266, Article 112596.
<https://doi.org/10.1016/j.oceaneng.2022.112596>

This material is protected by copyright and other intellectual property rights, and duplication or sale of all or part of any of the repository collections is not permitted, except that material may be duplicated by you for your research use or educational purposes in electronic or print form. You must obtain permission for any other use. Electronic or print copies may not be offered, whether for sale or otherwise to anyone who is not an authorised user.



CFD predictions of unsteady cavitation for a marine propeller in oblique inflow

Ville Viitanen ^{a,*}, Tuomas Sipilä ^{b,1}, Antonio Sánchez-Caja ^a, Timo Siikonen ^c

^a VTT Technical Research Centre of Finland Ltd, 02150 Espoo, Finland

^b ABB Marine and Ports, 00980, Helsinki, Finland

^c Department of Mechanical Engineering, Aalto University, 02150 Espoo, Finland

ARTICLE INFO

Keywords:

Hydrodynamic cavitation
Marine propeller cavitation
Propeller hydrodynamics
Propeller-induced pressure pulses
Compressible two-phase flow

ABSTRACT

In this paper the Potsdam Propeller Test Case is numerically investigated in oblique inflow conditions. We consider three different topics: open water performance curves, cavitation observations, and pressure pulses induced by the propeller to the ceiling of the cavitation tunnel. In the oblique flow case, the inflow is not uniform from the perspective of the propeller, which results in the dependency of the propeller blade loading and cavitation on the blade rate frequency. The numerical simulations were compared to experimental results for each investigated case. Additionally, we analyzed the unsteady features of the cavitation on the blades as well as the pressure peaks in the propeller wake due to collapsing cavities. We found that the global performance and cavitation patterns close to the blades agree well with the tests in the numerical simulations. The agreement with the tests for the pressure pulses on the tunnel ceiling was better in the non-cavitating case. The unsteady cavitation shed behind the propeller and the subsequent collapse events induced a vast increase in recorded maximum pressure values. Root cavitation collapse produced pressure pulses an order of magnitude greater than the collapse of tip vortex cavitation. Also the collapse of cavities on the blades contributed to a significant increase in the pressure fluctuations on the blades.

1. Introduction

Cavitation in marine propellers can appear in different forms. Both steady and highly transient cavitation phenomena can be observed under typical operating conditions, e.g. attached sheet cavitation on the blade surface, transient bubble or cloud cavitation on the blade or in the wake, and vortex cavitation on the propeller tip and hub. Many adverse consequences can follow from cavitation in addition to degradation of performance, such as erosion, vibration, and underwater noise. Therefore, there is a need for accurate cavitation monitoring and control using experimental and numerical methodologies.

Numerical methods based on solving Reynolds-averaged Navier–Stokes (RANS) equations and those using large eddy simulation approaches have been successfully applied for assessing propeller hydrodynamic performance, including cavitation characteristics. Nowadays, numerical investigations of propeller operation in uniform open-water conditions show that very good accuracy in prediction of global forces, blade flow phenomena and also near-blade cavitation patterns is usually attainable. More realistic situations such as oblique flow and in-behind conditions are typically also included in the performance

assessments of propellers. The reliability, accuracy and feasibility when analyzing such operating conditions are paramount topics, for which careful validation of a range of flow phenomena is a requisite to assure that correct and relevant physics are reproduced by the flow solvers. Specifically, propeller cavitation has received growing attention, and a number of publications have reported investigations using high-fidelity numerical methods (Lloyd et al., 2017; Yilmaz et al., 2018, 2019; Morgut et al., 2019; Gaggero and Villa, 2018; Asnaghi et al., 2017). Several rather complex phenomena have been addressed, such as vortex cavitation and its inception (Asnaghi et al., 2018), hull pressure pulses (Ge et al., 2020), bubbly or cloudy cavitation (Viitanen et al., 2020a), erosion (Eskilsson and Bensow, 2015) and even shock waves (Budich et al., 2015). Strong Reynolds number effects on the flow patterns have been reported in special configurations like tip-loaded propellers (Sánchez-Caja et al., 2014), which is indicative of their potential to affect cavitation inception and development. In fact, such effects on propeller cavitation have been recently studied (Viitanen et al., 2020a), showing that the cavitation extent can be greater in full-scale conditions. Similar impacts can be expected

* Corresponding author.

E-mail address: ville.viitanen@vtt.fi (V. Viitanen).

¹ Formerly, VTT Technical Research Centre of Finland Ltd., Finland.

in other complex configurations like those leading to propeller–hull vortices (Martio et al., 2011). The evaluation of propeller-induced underwater noise, also in cavitating conditions, has been receiving increasing attention (Sakamoto and Kamiirisa, 2018; Ando et al., 2018; Lidtke et al., 2016; Viitanen et al., 2018; Sezen et al., 2020; Wang et al., 2022). Additionally, open-source computational fluid dynamics (CFD) tools are gaining more popularity, and, for instance, the inclined inflow case we consider in this paper has been studied earlier by Morgut et al. (2019) and Gaggero and Villa (2018), who used the open source toolbox OpenFOAM (OpenFOAM, 2016) for their predictions. Morgut et al. utilized several different mass-transfer models implemented in OpenFOAM, and focused on their qualitative performance for different cavitating conditions in uniform and oblique flow. Gaggero et al. analyzed the oblique flow cases with also a boundary element method (BEM), which were then compared to the RANS predictions together with a comprehensive evaluation of the smp'15 Workshop results (Kinnas et al., 2015). In addition to the cavitation dynamics, in this paper we assess the pressure pulses induced by the propeller in wetted and cavitating conditions. The pressure pulses in both the ceiling of the cavitation tunnel and in the propeller wake due to collapsing cavities are studied, which have not been covered in previous publications. Moreover, we use a compressible formulation for the flow equations, whereas previous studies have mainly employed incompressible solvers also for predictions of cavitation dynamics.

In this paper, we study numerically the propeller in oblique inflow conditions. The test we use is that analyzed in the smp'15 Workshop (Kinnas et al., 2015), that is, the Potsdam propeller test case (PPTC) in oblique inflow. The propeller axis is inclined by 12° with respect to the uniform inflow. The propeller operation in non-uniform flow differs greatly from the uniform axial inflow, since in the inclined case, the inflow velocity to the propeller plane has a perpendicular component in addition to the axial one. When viewed in terms of the propeller relative velocities, this causes the resultant flow to the propeller blade to be non-uniform with respect to the propeller rotation (nominal inflow). Additionally, the effective inflow has been demonstrated to deform in a dipole-like manner (Sánchez-Caja et al., 2021).

This paper is organized as follows: the flow solution is briefly outlined in Section 2; for a more comprehensive description we refer to other publications. A description of the studied cases is given in Section 3. The numerical results are presented and compared to the cavitation tunnel experiments in Section 4, where we first show the open-water characteristics and the cavitation observation of the propeller in various operating conditions, and compare our simulations to experimental findings. We then analyse the pressure pulses in the cavitation tunnel ceiling and compare the simulation to experiments. Lastly, we investigate pressure variations on the blades and in the wake due to unsteady cavitation structures. Finally, conclusions are drawn in Section 5.

2. Flow solution

2.1. Governing equations

Our flow model is based on a compressible form of the RANS equations where an assumption is made on the homogeneity of the fluid mixture among the different phases involved in the computation (Miettinen and Siikonen, 2015; Viitanen and Siikonen, 2017). Including the energy equations for the solution allows prediction of the correct acoustic signal speeds. The governing continuity and momentum equations are

$$\begin{aligned} \frac{\partial \alpha_k \rho_k}{\partial t} + \nabla \cdot \alpha_k \rho_k \mathbf{V} &= \Gamma_k, \\ \frac{\partial \rho \mathbf{V}}{\partial t} + \nabla \cdot \rho \mathbf{V} \mathbf{V} + \nabla p &= \nabla \cdot \boldsymbol{\tau}_j + \rho \mathbf{g}, \end{aligned} \quad (1)$$

where p is the pressure, \mathbf{V} the absolute velocity in a global non-rotating coordinate system, $\boldsymbol{\tau}_{ij}$ the stress tensor, α_k a void (volume) fraction of phase k , ρ_k the density, t the time, Γ_k the mass-transfer term, and \mathbf{g} the gravity vector. The void fraction is defined as $\alpha_k = \mathcal{V}'_k / \mathcal{V}'$, where \mathcal{V}'_k denotes the volume occupied by phase k of the total volume, \mathcal{V}' . For the mass transfer, $\sum_k \Gamma_k = 0$ holds, and consequently only a single mass-transfer term is needed. The energy equations for phase $k = g$ or l , the indices referring to gas (g) and liquid (l) phases, are written as

$$\begin{aligned} \frac{\partial \alpha_k \rho_k (e_k + \frac{V^2}{2})}{\partial t} + \nabla \cdot \alpha_k \rho_k (e_k + \frac{V^2}{2}) \mathbf{V} &= \\ -\nabla \cdot \alpha_k \mathbf{q}_k + \nabla \cdot \alpha_k \boldsymbol{\tau}_{ij} \cdot \mathbf{V} + q_{ik} + \Gamma_k (h_{k\text{sat}} + \frac{V^2}{2}) &+ \alpha_k \rho_k \mathbf{g} \cdot \mathbf{V}. \end{aligned} \quad (2)$$

Here, e_k is the specific internal energy, \mathbf{q}_k the heat flux, q_{ik} interfacial heat transfer from the interface to phase k , and $h_{k\text{sat}}$ saturation enthalpy. Since $\sum_k \Gamma_k = 0$, by adding the energy equations together, the following relationship is obtained between the interfacial heat and mass transfer,

$$\Gamma_g = -\frac{q_{ig} + q_{il}}{h_{g\text{sat}} - h_{l\text{sat}}} \quad \text{and} \quad q_{ik} = h'_{ik} (T_{\text{sat}} - T_k). \quad (3)$$

Above, h'_{ik} is a heat transfer coefficient between the phase k and the interface. In the case of a homogeneous flow, the resulting sound speed c for a two-phase mixture is obtained from the eigenvalues of the Jacobian of the flux vector as

$$\frac{1}{\rho c^2} = \frac{\alpha}{\rho_g c_g^2} + \frac{1-\alpha}{\rho_l c_l^2} \quad \text{and} \quad \frac{1}{c_k^2} = \frac{\partial \rho_k}{\partial p} + \frac{1}{\rho_k} \frac{\partial \rho_k}{\partial h_k}. \quad (4)$$

In the expressions above, h_k denotes the enthalpy of phase k . The momentum and total continuity equations in the homogeneous model do not change, except for the material properties like density and viscosity. They are calculated for the mixture as a weighted sum by the phase volume fractions, which are calculated as

$$\rho = \sum_k \alpha_k \rho_k \quad \text{and} \quad \mu = \sum_k \alpha_k \mu_k, \quad (5)$$

where μ is the dynamic viscosity. The turbulence effects are those of single-phase models for the mixture with material properties derived from the pressure and temperatures of the individual phases. The determination of the material properties is described in Miettinen (2007). The simulations were conducted with the general-purpose CFD solver FINFLO. The finite volume method is utilized to discretize the governing equations. The solution method is a segregated pressure-based algorithm where the momentum equations are solved first, and then a pressure–velocity correction is made. The velocity–pressure coupling is described in more detail in Viitanen and Siikonen (2017) and Viitanen et al. (2018). A physical time step corresponding to half a degree of propeller rotation was used in all the simulations, and approximately one hundred inner iterations were required within each physical time step. The viscous fluxes as well as the pressure terms are centrally differenced. For the convective part, the variables on the cell surfaces are evaluated using a third-order upwind-biased monotonic upstream-centered scheme for conservation laws (MUSCL) interpolation. A compressive flux limiter has been shown to improve the predicted tip vortex cavitation pattern (Viitanen and Siikonen, 2017), and such is applied for the void fraction in the present study. For the time derivatives, a second-order three-level fully implicit method is used. The flow solver is efficiently parallelized on multicore workstations and HPC clusters and in this study, 16–72 processors were used in the simulations depending on the case.

2.2. Turbulence modelling

The turbulence closure applied in the present calculations is the SST $k - \omega$ model (Menter, 1994). That is a zonal model, referring to the formulation where the $k - \omega$ equations are solved only inside the boundary layer, and the standard $k - \varepsilon$ equations, transformed to the

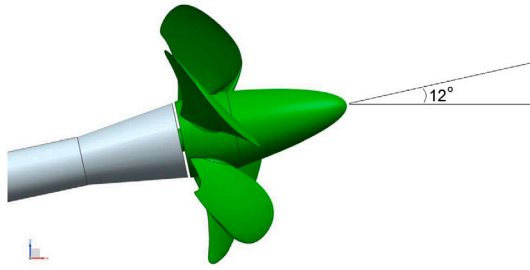


Fig. 1. Illustration of the inclination of the propeller axis with respect to the uniform inflow.



Fig. 2. Photograph of the PPTC propeller.

ω -formulation, are solved away from the walls. The calculations are performed up to the wall both in the model- and full-scale simulations, avoiding the use of wall functions. The height of the first cell was adjusted such that the non-dimensional wall distance $y^+ = \rho u_\tau y / \mu \lesssim 1$ for the first cell, with $u_\tau = \sqrt{\tau_w / \rho}$ being the friction velocity, τ_w the wall shear stress, and y is the normal distance from the solid surface to the center point of the cell next to the surface.

2.3. Mass and energy transfer

A number of mass-transfer models have been suggested for cavitating problems. Usually, the mass-transfer rate is proportional to a pressure difference from a saturated state or to a square root of that. In this study, we employ a mass-transfer model that is similar to that of Choi and Merkle (1993), described in Viitanen and Siikonen (2017) and Viitanen et al. (2020a). The empirical parameters of the cavitation model are calibrated by Sipilä (2012) for propeller flows, which were set equal to 370 for both vaporization and condensation. The saturation pressure is based on the free-stream temperature, and the gas phase was assumed to be saturated. The interfacial heat transfer coefficients are based on the mass-transfer model by assuming a saturated temperature for the gas phase, and the heat transfer is then determined by the mass-transfer model.

3. Test case

The investigated propeller is the VP1304, also known as the PPTC. The PPTC is a model-size controllable pitch propeller with a diameter of 0.250 m. The five-bladed propeller has a right-handed direction of rotation. The skew of the propeller is moderate. Table 1 summarizes the main geometrical parameters of the PPTC propeller, and a photograph of the propeller is shown in Fig. 2. The propeller operates in pull configuration. We performed the investigations according to the Propeller Performance Workshop of smp'15 Symposium of Marine Propulsors (Kinnas et al., 2015). The Workshop included predictions of the open-water curves of the propeller, cavitation observations at three different operating points, and pressure pulses induced by the propeller at three different locations and operating points. These are described in Sections 3.1–3.3. Where appropriate, we compare our present simulations to other numerical predictions, summarized by Kinnas et al. (2015). The numerical analyses reported in Kinnas et al. (2015) were blind tests, and only few global performance characteristics and cavitation sketches regarding these cases were released to the participants prior to the Workshop.

3.1. Case 1: Propeller open-water curves

The open-water performance of the PPTC propeller is analysed in oblique flow with the advance number range of $J = 0.6, \dots, 1.4$ with the interval of $\Delta J = 0.2$. The advance number is defined as

$$J = \frac{V_A}{nD}, \quad (6)$$

Table 1

Main geometric parameters of the PPTC propeller.

Diameter m	0.250
Pitch ratio at $r/R = 0.7$	1.635
Chord length at $r/R = 0.7$	0.417
Expanded area ratio	0.779
Skew [°]	18.837
Hub ratio	0.300
Number of blades	5
Direction of rotation	Right handed
Type	CPP

where V_A is the speed of advance with 12° inclination with respect to the propeller rotation axis (Fig. 1), $n = 15$ 1/s the rate of revolution and $D = 0.25$ m the diameter of the propeller. The thrust and torque of the propeller are non-dimensionalized as

$$K_{T_i} = \frac{T_i}{\rho n^2 D^4} \quad \text{and} \quad K_Q = \frac{Q}{\rho n^2 D^5}, \quad (7)$$

where T_i denotes the thrust, or force, in the i -direction ($i = x, y$ or z), and Q is the torque of the propeller about the propeller axis. In the results, a local coordinate system is used where the x -axis is aligned with the inclined propeller shaft, and the y -axis pointing to left and the z -axis up. The open-water efficiency of the propeller is defined as

$$\eta_0 = \frac{J}{2\pi} \frac{K_{T_x}}{K_Q}. \quad (8)$$

3.2. Case 2: Cavitation observations

The cavitation tests were conducted in the cavitation tunnel on in oblique flow. The simulations were conducted with a constant rate of revolutions of $n = 20$ 1/s and with three sets of different advance and cavitation numbers. The propeller was positioned in the cavitation tunnel as shown in Fig. 3. In the results, a local coordinate system is used where the x -axis is aligned with the inclined propeller shaft, and the y -axis pointing to left and the z -axis up. The cavitation number based on n is defined as

$$\sigma_n = \frac{p - p_{sat}}{\frac{1}{2} \rho (nD)^2}, \quad (9)$$

where p_{sat} is the saturation vapour pressure. We investigate three cases with different advance and cavitation numbers. The cases are listed in Table 2. The advance number $J = 1.269$ is the propeller design point. The other tested performance points $J = 1.019$ and $J = 1.408$ are off-design points on both sides of the design point.

3.3. Case 3: Propeller-induced pressures pulses

The configuration of the propeller in the cavitation tunnel is the same as in the previous case, that is, in oblique flow, but with the exception that the propeller is lifted closer to the ceiling of the tunnel, as shown in Fig. 4. The gap between the propeller tip and the ceiling of

Table 2
Advance and cavitation numbers of the simulated cases.

Case	J	σ_n
Case 2.1	1.019	2.024
Case 2.2	1.269	1.424
Case 2.3	1.408	2.000

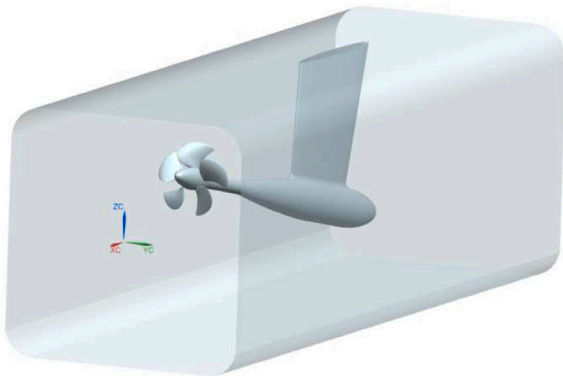


Fig. 3. Schematic view of the propeller in the cavitation tunnel for the second case.

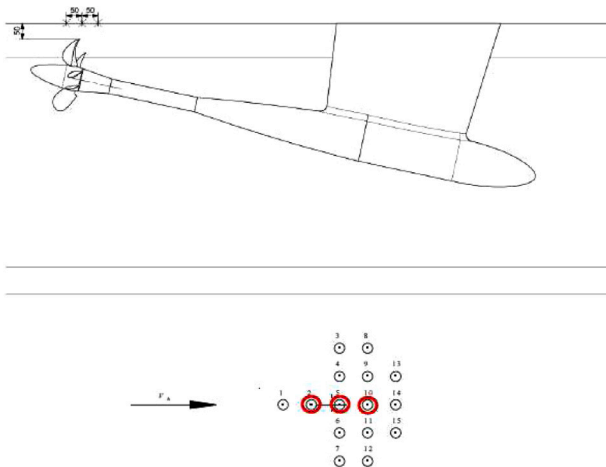


Fig. 4. Schematic view of the propeller in the cavitation tunnel for the third case. The lower figure shows the pressure sensors located above the propeller, on the ceiling of the cavitation tunnel. The sensors circled with red are considered in the Workshop.

the cavitation tunnel is 50 mm. Three pressure sensors are considered in the Workshop, and they are denoted as Sensors 2, 5 and 10 in Fig. 4. The sensors are located in the centre plane of the propeller axis, on the ceiling of the cavitation tunnel. Sensor 5 is located at the propeller plane, Sensor 2 being ahead, and 10 behind Sensor 5. The horizontal distance between each sensor is 50 mm. The advance and cavitation numbers are the same as in the previous case, see Table 2.

3.4. Grids and boundary conditions

In the open-water analyses the propeller was operated in pull configuration, i.e., the shaft was located behind the propeller. The blades, hub and shaft were modelled according to their IGES files. The strut from which the propeller shaft emerges was not modelled for the present simulations, since its influence on the propeller was considered negligible as it is located roughly three-and-a-half propeller diameters downstream of the propeller plane. We used an in-house grid generator to construct the structured multiblock grids, and the surface grids were generated with Numeca IGG. Three grid densities were used in the open

Table 3
Summary of the details of the grid used in the open-water calculations for the three grid levels. The number of surface cells is given for one side of the blade.

	Fine grid	Medium grid	Coarse grid
Total number of cells	21 347 840	2 668 480	333 560
Surface cells in chordwise direction	144	72	36
Surface cells in spanwise direction	104	52	26

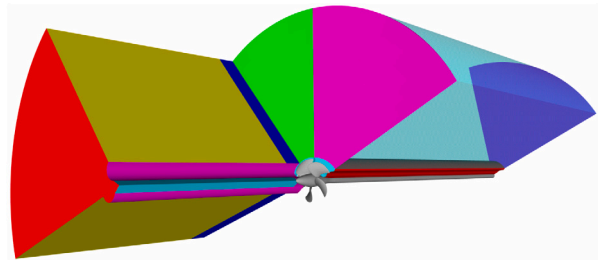


Fig. 5. Computational domain in the open-water calculations. The propeller, hub and shaft are coloured grey. The inlet face is coloured red, and the outlet face is coloured purple. Note that only a fifth of the block is shown, while the propeller, hub and shaft are shown whole. (For interpretation of the references to colour in this figure legend, the reader is referred to the web version of this article.)

water calculations. The details are summarized in Table 3. The grid has an O-O topology around the propeller blades. The finest grid levels consist of roughly 21 million cells in 90 blocks. The grid resolution around the leading edge is fine, and there are about 30 cells around the leading edge radius. Due to the O-O topology, the same resolution was applied around the blade tip and the trailing edge as well. The grid was refined normal to the viscous surfaces such that $y^+ \approx 1$ at the finest grid level. The grid details near the propeller were the same for all three cases.

The computational domain for Case 1 is shown in Fig. 5. Due to the time-dependent nature of the problem, the whole propeller was modelled in the inclined flow calculations. The inlet is located five diameters upstream of the propeller, and the outlet is located ten diameters downstream of the propeller. The outer sides of the cylindrical domain are located four diameters from the propeller in the radial direction, and their effect is negligible in the calculations.

The blades, hub and shaft were modelled as no-slip rotational surfaces. A velocity boundary condition was applied at the inlet, and a pressure boundary condition was applied at the outlet. The outer side of the domain has a free-stream boundary condition. The whole computational domain is rotation with the given rate of rotation. The inflow velocity was set based on the advance numbers of the propeller.

The calculations were performed on three grid levels for the Case 1. For the coarser grid levels, every second point was taken into account compared to the finer level grid. A quasi-steady solution was used as an initial guess for the time-accurate calculations on each grid level. A grid density study was not performed using any systematic method, such as a Richardson extrapolation and typically, very little difference is expected in global forces predicted by medium and fine grid simulations near the design point of the propeller.

The grid for Case 2 was constructed based on the grid used for the first case and shown in Fig. 6. The geometry of the cavitation tunnel was provided in the IGES files. A sliding mesh technique was utilized to allow for the rotation of the propeller inside the tunnel, and a rotational no-slip boundary condition was used for the rotating solid surfaces. A no-slip boundary condition was applied on the tunnel walls. The computational domain used in Case 2 is shown in Fig. 7. The grid close to the propeller was the same as that used in the first case. The total number of cells on the first grid level is roughly 25 million in 103 grid blocks. However, we performed the calculations only on the second grid level, which consists of approximately 4 million cells. The shaft

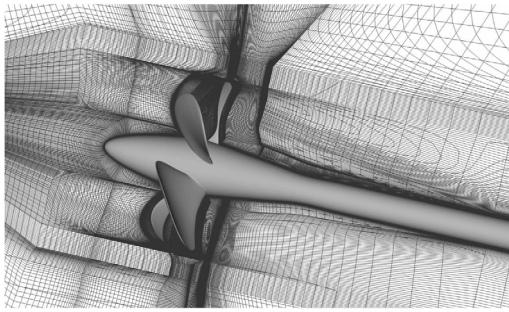


Fig. 6. View of the computational grid near the propeller along a cut on the center y -plane for the Case 2 grid.

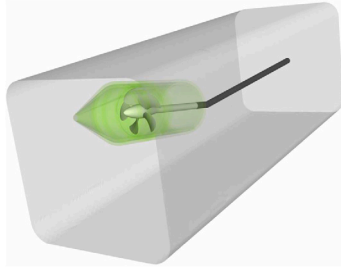


Fig. 7. Computational domain for the calculations in the cavitation tunnel for Case 2. The propeller, hub and shaft are coloured with grey. The green transparent parts denote the rotating blocks. (For interpretation of the references to colour in this figure legend, the reader is referred to the web version of this article.)

was extended to the outlet by turning it 12° roughly four diameters downstream of the propeller. The grid for Case 3 was created by lifting the grid near the propeller in Case 2 close to the tunnel ceiling so that the tip clearance was 50 mm. Calculations were performed only on the second grid level. The grids were built so that the second grid level was enough to get adequate resolution of especially propeller performance as well as cavitation phenomena based on our experience with standard computations of similar propeller cases. Our goal was also to keep the simulation costs for the wide range of investigated unsteady cases reasonable. A grid sensitivity analysis is thus excluded in this study. We note that Sipilä (2012) and Viitanen et al. (2020a), e.g., have performed a grid sensitivity study previously using the same flow solver, numerics and a similar grid construction methodology for the same propeller and operating conditions in wetted and cavitating cases, albeit in uniform flow.

4. Results

In this section, we present the results of the three different cases. We compare our results to the model tests, and to the CFD simulations performed by the other participants of the smp'15 Propeller Workshop (Kinnas et al., 2015). In Section 4.1 we validate the propeller open-water performance, and in Section 4.2 we analyze the predicted cavitation patterns together with experimental observations. In Section 4.3, the pressure pulses induced by the wetted and cavitating propellers are investigated. All iso-surfaces depicting the cavitation are in terms of the volume fraction $\alpha = 0.5$.

4.1. Case 1: Open water performance

The open-water curves and their comparison with the open-water tests are plotted in Figs. 8 and 9. Fig. 8 shows all the force coefficients, as well as the torque coefficient and the efficiency. The results are obtained on the finest grid. Fig. 8(a) also shows the model test results.

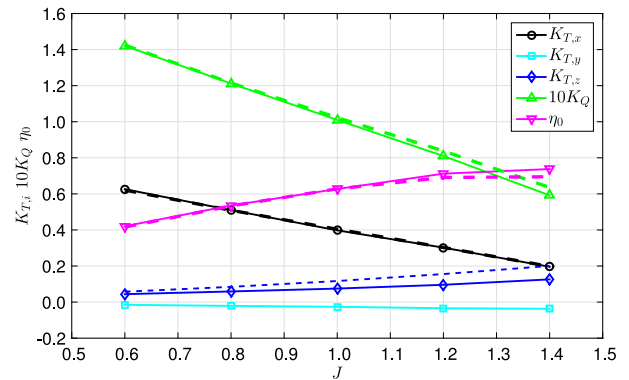


Fig. 8. Open water characteristics of the PPTC propeller in oblique flow. The dashed lines denote the corresponding results for $K_{T,x}$, K_Q and η_0 from the model tests. Eq. (10) is shown as the dashed blue line. The CFD results are from the finest grid. The experimental results are given in Kinnas et al. (2015). (For interpretation of the references to colour in this figure legend, the reader is referred to the web version of this article.)

Fig. 9 shows the relative difference between the computations and the model tests for the simulations on the fine, medium and coarse grids. Additionally, we plot in Fig. 8 the z -force acting in the propeller plane based on a simple momentum theory as proposed by Matusiak (2003), that is,

$$F_{p,z} = \frac{\rho A_p V_A^2 \left(\frac{1}{2} + \sqrt{1 + C_T/2} \right) / \cos \delta}{\rho n^2 D^4}, \quad (10)$$

where A_p is the propeller disk area, $C_T = 8K_T/(\pi J^2)$ and δ the propeller axis inclination, and for the thrust coefficients we used the experimental values. All open-water curves show smooth behaviour over the entire investigated advance number range. The coefficients $K_{T,x}$ and K_Q , and consequently η_0 , resemble closely the form of the typical open-water curves with axially uniform inflow. The side force coefficients are significantly smaller in magnitude, the $K_{T,z}$ being slightly larger than the $K_{T,y}$. The $F_{p,z}$ from Eq. (10) has a similar trend to the $K_{T,z}$, although the approach based on momentum theory predicts larger values for the force component especially for higher advance numbers. The magnitudes of both side force components increase as the propeller loading decreases. The open-water performance of the PPTC propeller is replicated reasonably well for the four first advance coefficients. When compared to the open-water tests, the differences are within four per cent for the four first operating points. The highest advance number shows increased discrepancy with the model tests and computations, and the deviation in the CFD predictions rises to seven per cent for the torque coefficient, and the efficiency. The deviation in the thrust coefficient, however, remains smaller. We note that the point $J = 1.4$ presented the greatest deviation also in the computations performed by the other participants of the Workshop. In principle, the higher the advance number, the higher uncertainty expressed in percentage for both the measurements and computations due to the decreasing magnitude of the performance coefficients. Interestingly, errors present in the results of the coarser grids seem under certain conditions to cancel out in the sense that the resulting propeller open-water efficiency is actually in better agreement with the experimental values than on the fine grid, even though the thrust and torque coefficients on the finest grid are mainly very close to the experimental values. On the finest grid throughout the investigated range of advance coefficients, better agreement is seen in the thrust coefficients, while the torque coefficients exhibit greater deviations. On the coarser grids, the percentage differences of $K_{T,x}$ and K_Q are similar in magnitude for each J , and consequently also the differences in η_0 remain comparable.

Examples of the time histories of the force coefficients are plotted in Fig. 10. The forces acting on the whole propeller reach a steady level at

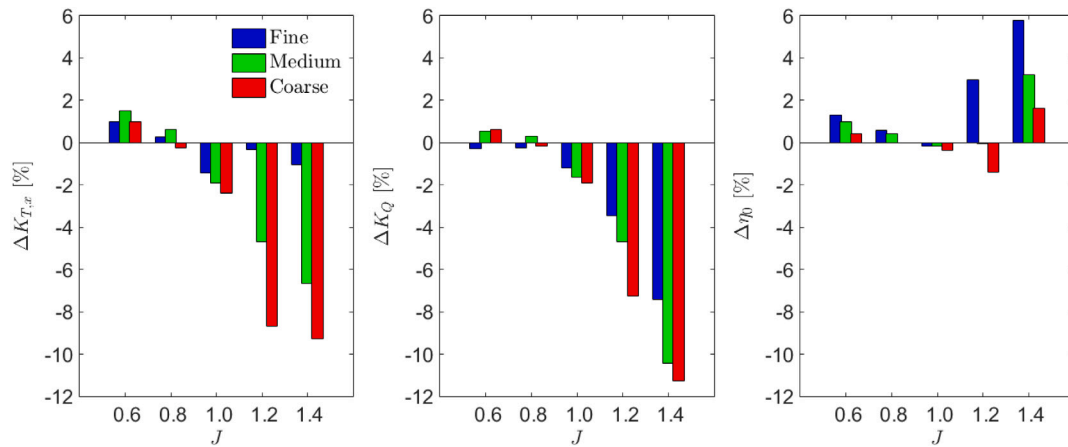


Fig. 9. Percentage differences of propeller open-water characteristics for fine, medium and coarse grid simulations with respect to the experimental values. On the left: thrust coefficient. Middle: torque coefficient. On the right: open-water efficiency.

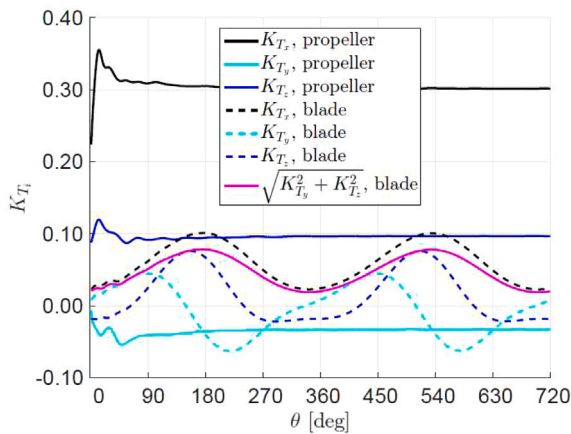


Fig. 10. An example of the time histories of the thrust coefficients of the whole propeller and a single blade. The advance number is $J = 1.2$.

around three-quarter revolutions. The coefficients for the single blade seem, however, to attain a periodic form slightly earlier, at around half a revolution. We extended the simulations to at least two full propeller revolutions, or to ten blade passings, to ensure the convergence. Computations made with the other advance numbers show a similar behaviour. The K_{T_x} value for a single blade exhibits a distinct sinusoidal behaviour. The in-plane components do not show a similar linear behaviour in this plot, but the resultant in-plane force for a single blade shows the sinusoidal shape, as shown in Fig. 10.

4.2. Case 2: Cavitation observations

Figs. 11 and 12 show the cavitation patterns of the propeller at the three operating points, together with cavitation sketches from the experiments. Examples of the time histories of the force coefficients of the whole propeller and a single blade are plotted in Fig. 13 for Case 2.1 conditions. In addition, we show a more detailed comparison of the cavitation dynamics at various blade positions between EFD and CFD in Figs. 14–16 for Cases 2.1, 2.2 and 2.3, respectively. These figures show one blade passage, or 72° of propeller rotation at 12 degree intervals. The experimental video recordings we used in these figures were obtained from <https://www.sva-potsdam.de/smp15-propeller-workshop/>.

Case 2.1 exhibits sheet, bubble and tip vortex cavitation on the suction side, in addition to root cavitation. The strong cavitating tip

vortex is present both in the simulations and in the model tests. The root cavitation is also present in the simulations. The extent of the sheet cavitation on the blades is significantly greater in the simulations than in the model tests, although we observe extensive bubble cavitation occurring in the experiments. We note that the extent of the pressure side cavitation is very small both in the simulations and in the model tests. As the blades begin to ascend from the top-dead centre, the root and bubbly cavitation on the blades are highly dynamic, disappearing fast with the ascending blades. This is due to the variations of the angle of attack of the blades, that is, the varying blade loading. Cavity structures are then shed in the wake. The sheet or bubbly cavitation types are subsequently absent as the blades have passed the bottom-dead-centre, and begin to ascend. We observe that the cavitating tip vortex is strongest around $\theta \approx 90^\circ$. Also the modes of the tip vortex cavitation are captured in the simulations. The extent of the tip vortex cavitation is, then again, limited in the simulations owing to the coarsening of the grid. Due to this, the cavitating tip vortex breaks into several segments for some blades as the propeller rotates.

Case 2.2 also shows tip vortex cavitation, and the sheet and root cavitation appear now on the pressure side during the ascending of the blades. Bubbly cavitation covers most of the blade suction side as it descends, and the simulations predict this as quite extensive sheet cavitation. Very dynamic cavity structures are shed into the wake from the pressure side root cavitation as well as from the suction side bubble or sheet cavitation. In the experiments, we note that these structures extend some distance in the wake, while the cavitation collapses earlier behind the propeller in the simulations. Again, this is due to the coarsening of the grid. Similarly as earlier, the cavitating tip vortex is strongest around $\theta \approx 90^\circ$, and the modes of the tip vortex cavitation are captured in the simulations. The extent of the cavitation is limited due to the coarsening of the grid.

For Case 2.3, the sheet cavitation on the pressure side grows to a greater extent and then joins the tip vortex cavitation. The suction side now exhibits root cavitation. A fine tip vortex cavitation is visible in the experiments and in the simulations. The pressure side sheet cavitation appears as the blade ascends towards the top-dead-centre. As the blades begin to descend, this sheet cavitation disappears very rapidly at similar angular positions in the experiments and in the simulations. Then, merely pressure side root cavitation is present until we again approach the top-dead-centre, which continues to shed cavitation structures in the wake. The closure of the pressure side sheet cavitation is foamy in the experiments, whereas it appears more distinctly in the simulations. The suction side now exhibits root cavitation both in the experiments and in the simulations, its extent being the greatest at around $\theta \approx 90^\circ$.

The leading edge cavitation on the suction side for Case 2.1 incepts already close to the 12 o'clock position, in addition to the small root

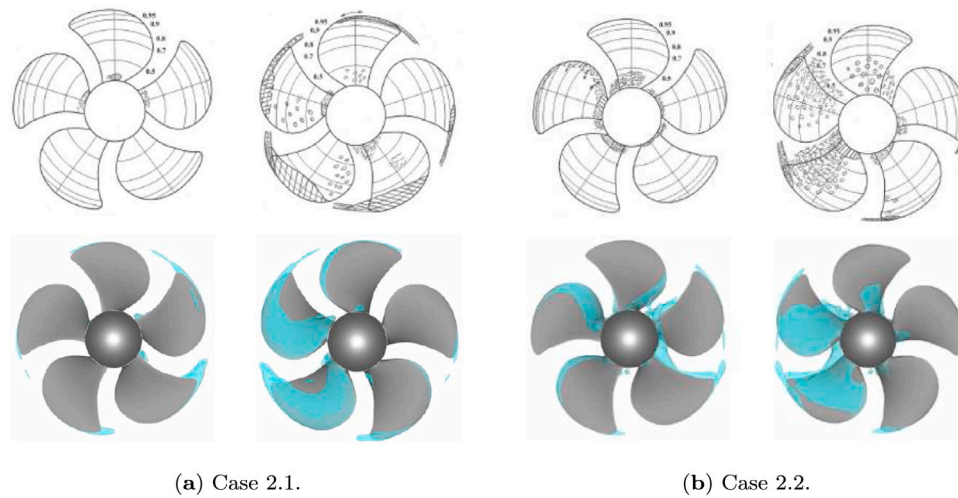


Fig. 11. Comparison of the cavitation patterns between the model tests and the computations. The top row shows the EFD and the bottom row the CFD results. Left figures: pressure side; right figures: suction side. The experimental results are reproduced from Kinnas et al. (2015).

cavitation. In the experimental findings this was slightly delayed and confined closer to the tip. The simulations tend to promote the turbulence earlier than the model tests near the leading edge of the blade. In tests, the transition from laminar to turbulent flow is delayed on a smooth blade, and consequently the cavitation inception can be delayed too. In a full-scale propeller, the turbulent fluctuations of the pressure further promote the inception of cavitation, in regions where the local pressure is close to the vapour pressure. The observed absence of sheet cavitation in the model test is likely caused by laminar flow near the leading edge. In the experiments, the region between the leading edge and the mid-chord is covered with bubble cavitation at $\theta = 90^\circ$. Having passed the bottom-dead-centre, neither root nor sheet cavitation is present on the suction side of the blade in the simulations at $\theta = 270^\circ$. Similarly for the other operating conditions, the pressure side sheet cavitation incepts earlier in the simulations than in the experiments as the blade ascends. The severity of the leading edge cavitation in the simulations increases as the blade descends for Case 2.1 or ascends for Cases 2.2 and 2.3. In the regions where the angle of attack is increased, the cavitation extent on the suction side is the highest in all three operating conditions. Also, we observe that as the blade angle of attack increases, the suction side sheet cavitation dominates at the two highest loading conditions. Conversely, in regions where the angle of attack is decreased, the suction side cavitation mostly vanishes. The decreasing angle of attack causes pressure side cavitation at $J = 1.269$ and $J = 1.408$. The extent of the pressure side cavitation increases with the increasing advance number. In the highest loading condition, there is next to no pressure side cavitation except for the small area near the root. Lastly, as we have shown earlier (e.g., in Viitanen and Siikonen (2017)), predicting certain types of cavitation dynamics is a challenge for URANS approaches. Cavitation patterns can be smeared due to excess eddy viscosity, and the unsteady behaviour can be affected. Naturally, also a finer grid spacing would allow us to extract a more detailed representation of the dynamics of the two-phase flow.

A comparison of the global performance characteristics between the model tests and the computations, in cavitating and wetted conditions, is given in Table 4. For Case 2.1, both in the cavitating conditions and in the wetted conditions, the calculated torque coefficients agree very well with the tests. The computed thrust coefficients for both cavitating and wetted conditions show slightly higher discrepancies. However, the differences are at most within 4 four per cent. Twenty submissions were made for this case (Kinnas et al., 2015), and the average difference is 3.9% with a standard deviation of 2.3%. The predicted thrust coefficient for the cavitating conditions of Case 2.2 shows a rather large difference. The prediction of the thrust breakdown

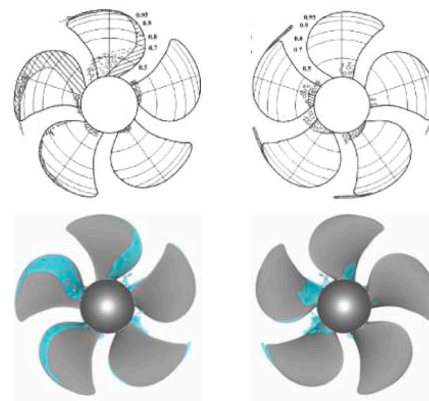


Fig. 12. Comparison of the cavitation patterns between the model tests and the computations for Case 2.3. The top row shows the EFD and the bottom row the CFD results. Left figures: pressure side; right figures: suction side. The experimental results are reproduced from Kinnas et al. (2015).

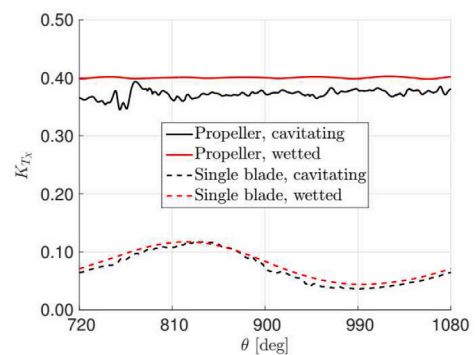


Fig. 13. An example of the time histories of the thrust coefficients of the whole propeller and a single blade in cavitating and wetted conditions.

at the design point appears difficult; it is here noted that similar large disparity is present in most submissions gathered in Kinnas et al. (2015), and the average difference between the seventeen participants

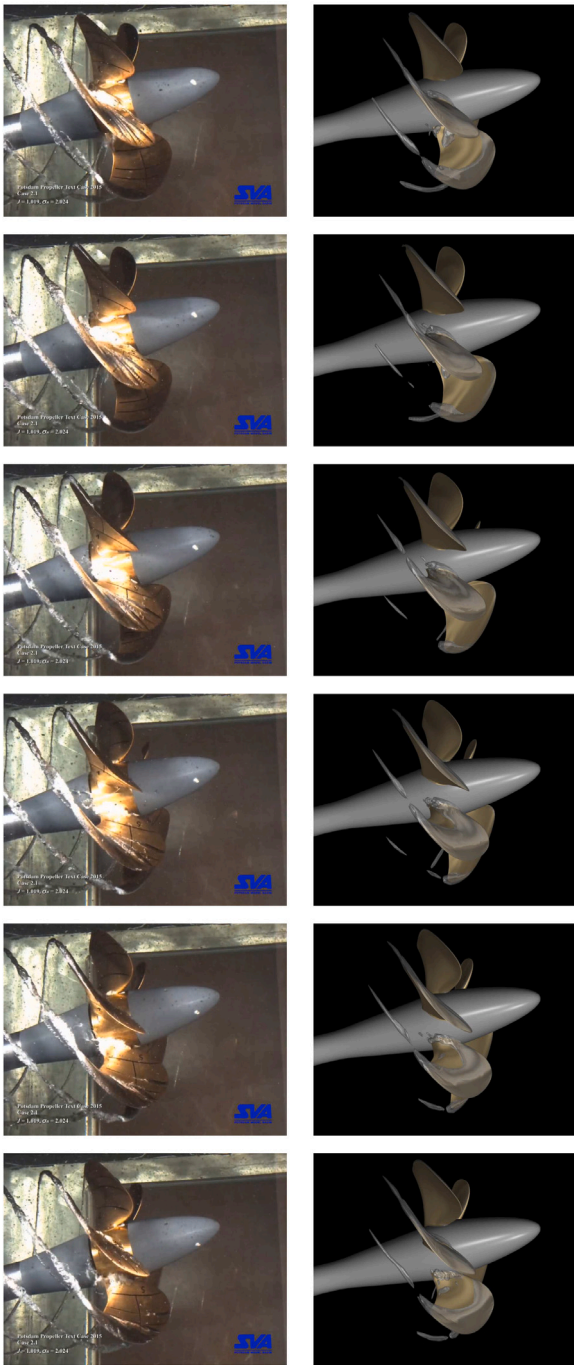


Fig. 14. Sequence of snapshots illustrating cavitation dynamics for Case 2.1. On the left: EFD; On the right: CFD. The angular interval between each frame is 12°.

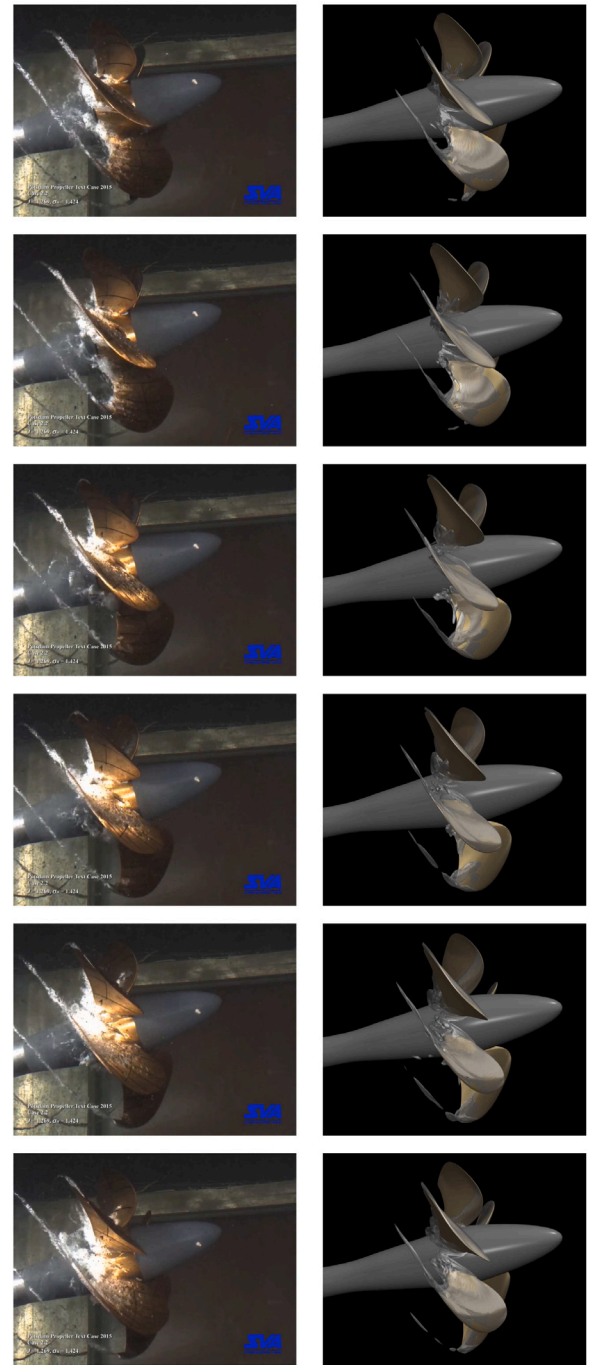


Fig. 15. Sequence of snapshots illustrating cavitation dynamics for Case 2.2. On the left: EFD; On the right: CFD. The angular interval between each frame is 12°.

is 18.7%. Additionally, the standard deviation between the results is rather wide, being 15.5%. Note as well that the prediction obtained for the thrust coefficient in the wetted condition agrees very well with the model tests.

Upon inspecting Fig. 11(b), we see that the cavitation extent in Case 2.2 is significantly greater than in the other two cases. Additionally, it mainly consists of bubble cavitation in the model tests. Bubble cavitation is not easily predicted using homogeneous two-phase models on practical grids. There are mass-transfer models that include the effects of bubble dynamics and turbulence, e.g. Muzafferija et al. (2017) employ a Rayleigh–Plesset relation with the mass-transfer modelling, and the model of Singhal et al. (2002) (sometimes referred to as

the full cavitation model) is active only in regions where the flow is turbulent. In the previous workshop, results bearing closer resemblance to the model tests were obtained using this model. However, Morgut et al. (2015) showed the best correspondence in the global forces was obtained using the Kunz et al. (2000) model and the Zwart et al. (2004) model. It is to be noted here that they also used the model of Singhal et al. (2002) to compute Case 2.2, but obtained better results, in terms of the thrust coefficient, with the two former models. We note that most of the participants predicted very similar sheet cavitation patterns, as is seen in Fig. 11(b). Results from all of the participants are given by Kinnas et al. (2015).

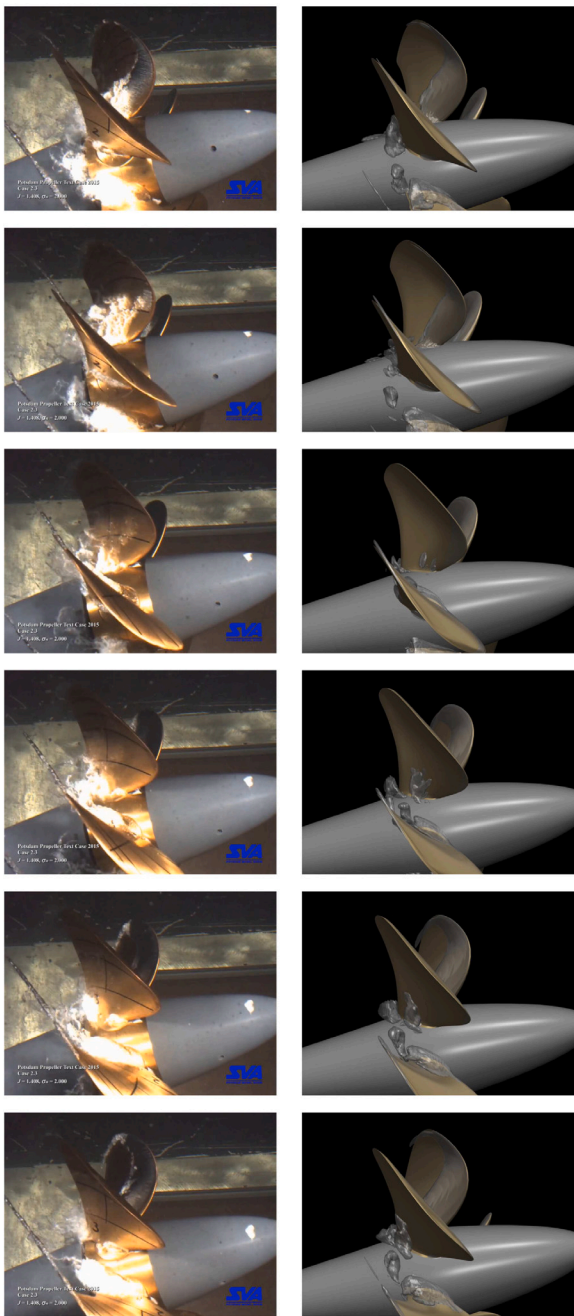
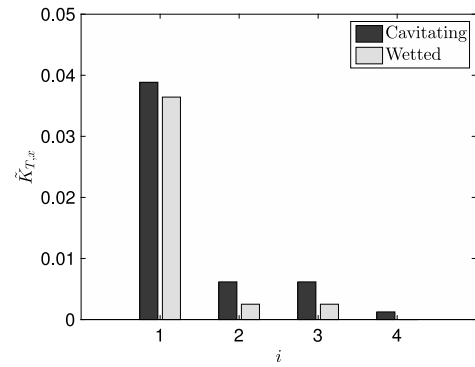


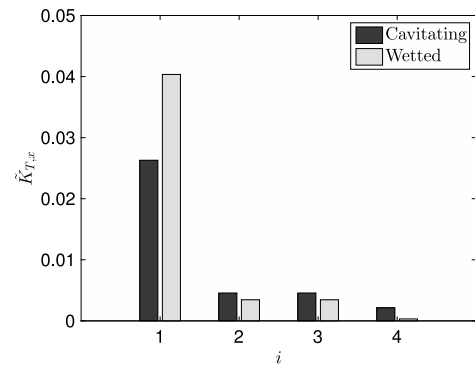
Fig. 16. Sequence of snapshots illustrating cavitation dynamics for Case 2.3. On the left: EFD; On the right: CFD. The angular interval between each frame is 12°.

In the wetted conditions for Case 2.3, the calculated thrust coefficient is the same as that obtained from the model tests. The computed thrust coefficients for the cavitating conditions show a difference of slightly under five per cent when compared to the model tests. Sixteen submissions were made for this case (Kinnas et al., 2015), and the average difference is 21.3% with a standard deviation of 17.5%.

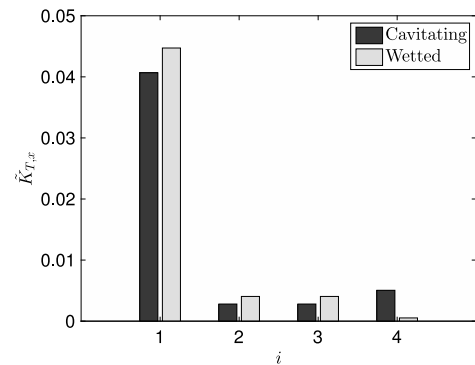
A comparison of the harmonic content, in terms of the blade frequency and its three higher order harmonics, of the thrust coefficients in cavitating and wetted conditions for Cases 2.1–2.3 is given in Fig. 17. As the inflow is unsteady from the perspective of the propeller, the signal is dependant on the blade-rate frequency. For Case 2.1 conditions, amplitudes of the thrust coefficients for a single blade are greater in cavitating than in the wetted conditions. For Case 2.2, the wetted conditions obtain higher amplitudes for the first harmonic component.



(a) Case 2.1.



(b) Case 2.2.



(c) Case 2.3.

Fig. 17. First and higher-order harmonic components of the cavitating and wetted thrust coefficients for a single blade.

The higher order harmonics, however, show greater amplitudes in the cavitating conditions. For Case 2.3, the wetted conditions obtain again higher amplitudes for the first harmonic component.

In the wetted and cavitating conditions, thrust coefficients of the propeller and the single blade converged to their final periodic values within two propeller revolutions. The thrust coefficients are more unstable in the cavitating conditions. This is due to the unsymmetric cavitation pattern that prevails in the non-uniform inflow condition (Figs. 11 and 12). The thrust coefficients of the whole propeller also attain slightly lower values in the cavitating conditions than in the wetted conditions. Examples of the time histories of the force coefficients of the whole propeller and a single blade are plotted in Fig. 13 for Case 2.1 conditions. The figure shows the third full revolution of the propeller in wetted and cavitating conditions.

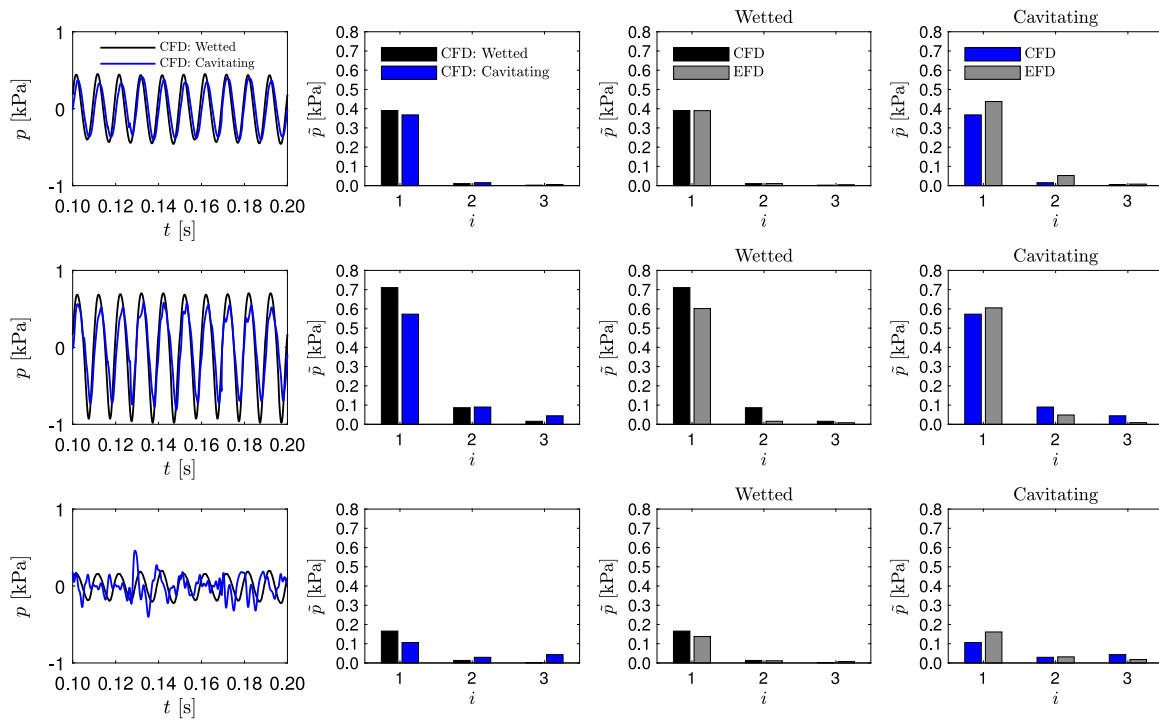


Fig. 18. Pressure pulses at the three sensors on the ceiling of the cavitation tunnel. The top row shows results from Sensor 2, middle row from Sensor 5 and bottom row from Sensor 10. First column: Pressure time histories obtained from CFD in wetted and cavitating conditions. Second column: Comparison of CFD predicted harmonics in wetted and cavitating conditions. Third and fourth columns: Comparison of EFD and CFD predicted harmonics in wetted and cavitating conditions, respectively. Black colour depicts the wetted case. Blue colour depicts the cavitating case. Grey colour denotes the experimental results. The i denotes the harmonic of the blade-passing frequency. The results from the model tests are provided in [Kinnas et al. \(2015\)](#). (For interpretation of the references to colour in this figure legend, the reader is referred to the web version of this article.)

Table 4

Comparison of the global performance characteristics between the simulations and the model tests. The model test results are given in [Kinnas et al. \(2015\)](#).

	Cavitating		Wetted	
	K_{T_x}	$10 \cdot K_Q$	K_{T_x}	$10 \cdot K_Q$
Case 2.1				
Test	0.363	0.959	0.392	1.005
Simulation	0.375	0.961	0.401	0.999
Difference	3.3%	-0.2%	2.3%	0.6%
Case 2.2				
Test	0.167	-	0.265	-
Simulation	0.192	0.595	0.266	0.737
Difference	15.0%	-	0.4%	-
Case 2.3				
Test	0.123	-	0.189	-
Simulation	0.129	0.474	0.189	0.579
Difference	4.9%	-	0.0%	-

4.3. Case 3: Propeller induced pressures pulses

We analyzed Case 3.1 within this study. The conditions in the cavitation tunnel were the same as for Case 2.1. [Fig. 18](#) shows the time histories of the pressures in all three sensors in the cavitating and wetted conditions. The first three harmonics of the signals are also shown, together with the corresponding results from the model tests. Six full propeller revolutions, or 30 propeller blade passages, were simulated. The model test results are provided by [Kinnas et al. \(2015\)](#). [Fig. 19](#) shows a series of snapshots from the simulations. The figure shows six time instants at 12° intervals covering one blade passage. Sensor 5 is located at the propeller plane, with Sensor 2 being ahead, and 10 behind sensor 5.

Observing the experimental results, we see that for all sensors the pressure pulses at the blade-passing frequency are notably greater

than the higher-order harmonics. The pressure amplitudes at Sensor 5 are the greatest, and the pressures at Sensor 10 are the lowest for both wetted and cavitating conditions. Also, the relative magnitudes of the higher-order harmonic components increase for Sensor 10, when compared to the pressure amplitudes at the blade-passing frequency. We note these trends also from the CFD predicted pressure amplitudes. In the experiments, the pressure pulses in wetted and cavitating conditions at Sensor 5 are quite similar in amplitude at the blade-passing frequency. The higher-order harmonics are greater in the cavitating case. The first and higher-order pressure amplitudes are greater in cavitating conditions for Sensors 2 and 10, although the increase when compared to the wetted case is not very large especially at the blade-passing frequency. CFD predictions yield greater pressure amplitudes in the wetted conditions at the blade-passing frequency. The higher-order harmonic components are, then again, greater in the cavitating case.

The pressure pulses measured by Sensor 2 agree rather well between the simulations and the model tests in the wetted conditions. All predicted harmonic components are fairly close to the experimental values. In the cavitating conditions, the amplitudes are slightly under-predicted compared to the model tests. The pressure pulses measured by Sensor 5 show a bit greater discrepancy between the simulations and the model tests in the wetted conditions. The harmonic components are over-predicted in the simulations. A similar trend, albeit less pronounced, is visible in the cavitating conditions. The amplitude at the blade-passing frequency is close to the experiments in the cavitating conditions, although the higher-order components are a bit under-predicted. The pressure amplitudes measured by Sensor 10 are also quite similar between the simulations and the model tests in the wetted conditions for the harmonic components. The amplitude obtained with CFD at the blade-passing frequency is again a bit under-predicted. The low pressure regions due to the cavitating tip vortex are slightly greater by extent than in the wetted conditions in [Fig. 19](#). Also the suction side low-pressure area near the bottom-dead-centre is larger in extent in cavitating conditions: a big region of sheet cavitation is present. As the

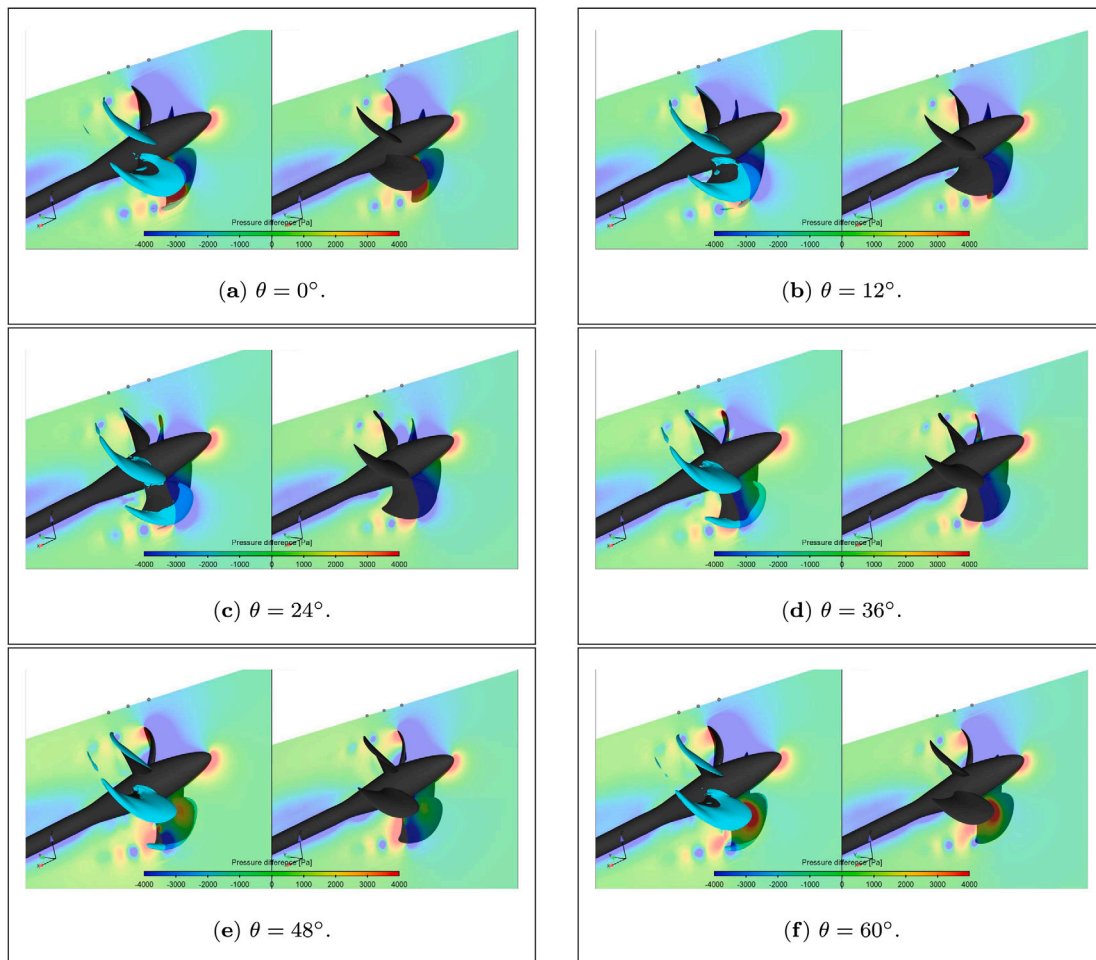


Fig. 19. Sequence of snapshots depicting the pressure difference on a centre cut plane of the tunnel. On the left: cavitating conditions, where cavitation is shown as the blue iso-surface. On the right: wetted conditions. (For interpretation of the references to colour in this figure legend, the reader is referred to the web version of this article.)

blades descend, the pressure distribution near the bottom-dead-centre appears more uniform in the wetted case, whereas for the cavitating case its values increase more rapidly near the propeller root region and undergoes oscillations close to the closure of the sheet cavitation. Now cavitation is present close to the top-dead-centre, and the pressure distributions are quite similar. We also note more fluctuations in the pressure near the propeller shaft for the cavitating case, which is due to the unsteady root cavitation.

4.4. Pressure distributions and cavitation dynamics on the blades

Here, we investigate the instantaneous pressure distributions for Case 2.1 on selected radii on the blades to reveal some consequences due to the unsteady characteristics of the propeller cavitation. To this end, also time histories of maximum values of the pressure coefficients in dedicated investigation zones behind the propeller are studied later in Section 4.5. The pressure distributions on the surfaces of the blade, and specifically on three different radii, as well as at six different angular positions are plotted in Figs. 20–21. Case 2.1 is investigated for both cavitating and wetted conditions. The studied radial locations were chosen to be $r/R = 0.4$, $r/R = 0.6$ and $r/R = 0.816$. We chose these locations based on animations made of the evolution of the blade surface pressure on several radial locations.

Fig. 20 shows the pressure distributions and cavitation extents for $\theta = 0^\circ - 144^\circ$. We note that cavitation incept slightly below the second radial location, where the pressure drops below the vapour pressure. Consequently, the blade surface pressures in the cavity are cut by the

vapour pressure. Otherwise, the pressure distributions are roughly the same; no sharp pulse is observable due to the initiating cavity. Now at $\theta = 72^\circ$ the sheet cavity covers most of the blade at all three radii, and consequently the surface pressure is again cut by the vapour pressure. This is confirmed by the plots of the wetted case. In the cavitating case, there is a slight jump in the pressure at the closure of the sheet cavity. This is caused by the streamlines that travel over the cavity and hit the blade surface behind the cavity. These jumps are, of course, absent on the blade of the wetted propeller. Note also that there is a visible pressure peak on the surface of the blade at $\theta = 216^\circ$, near the trailing edge of the cavitating propeller. This coincides with the smallest radius, and the peak is due to a collapsing sheet cavity on the blade; this is shown below. Again in the cavitating regions, at $\theta = 144^\circ$, the pressure is cut by the vapour pressure. This is again confirmed by the wetted propeller. Most of the blade of the cavitating propeller is covered with the sheet cavity. It is, however, observable, that the extent of this sheet cavity starts to decrease. Additionally, the thickness of the cavitating tip vortex is increasing. These were also confirmed from the animations. A rather large pressure peak is present near the trailing edge of the blade near the radius of $r/R = 0.6$; its origin is not entirely clear from the figure. Closer investigations on the pressure and vapour distributions on the blade revealed, however, that there appeared a cloud cavity that originates from the shedding process of the sheet cavity as the blade descends. The cloud cavity collapsed shortly after, *i.e.*, within just a few degrees. This blade position captures a snapshot of the pressure peak originating from this collapse. Note that there is a slight peak present also at the smallest radius in the cavitating case, which is due to the collapsing root cavities.

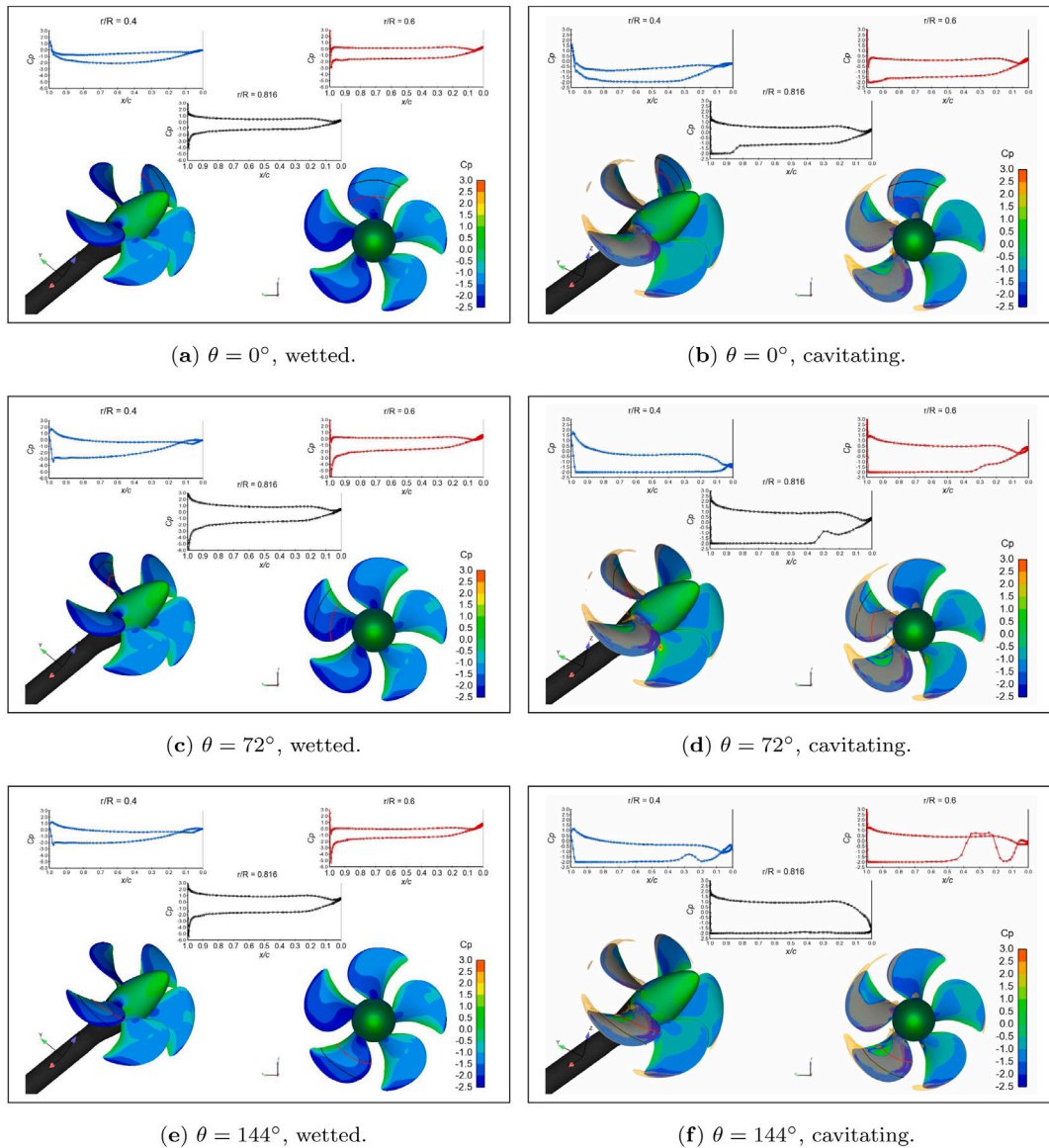


Fig. 20. Pressure distributions at various radii at $\theta = 0^\circ$. The orange transparent region denotes the iso-surface of $\alpha = 0.5$. $J = 1.019$ and $\sigma_n = 2.024$. Note the different scale for the y -axis in the plots for the wetted case. (For interpretation of the references to colour in this figure legend, the reader is referred to the web version of this article.)

Fig. 21 shows the pressure distributions and cavitation extents for $\theta = 180^\circ$ – 216° . The pressures on the surface of the wetted propeller are again smooth at mid-chord. In the cavitating case, the decreasing extent of the sheet cavitation seems to produce a small jump in the pressure distributions at the two largest radii at the cavity closure. Notable pressure peaks appear in the root of the cavitating propeller. These are visible in the pressure distributions at the smallest radius. It is seen that a rather large pressure peak is present at the root of the cavitating propeller. Judging from the previous figure, and also the closer inspections made for the incidence, this strong peak is again due to the collapse of the root cavities, especially close to the junction of the blade and the root. At $\theta = 190^\circ$ we see that the previously visible strong peak in near the root region has mostly vanished. However, there is some dynamic root cavity present near the smallest radius, which is visible in the pressure distribution. In addition, the rapid extinguishing of the leading edge sheet cavitation, especially close to the higher radius, produces a very strong local peak. This is captured in the pressure distributions at the largest radius. Based on the animations made for this case, the suction side sheet cavitation collapses very fast as the blade ascends beyond the bottom-dead-center, which is

confirmed by the snapshot. The extent of the extinguishing cavity seems to reach the middle radius as well. At $\theta = 216^\circ$ the distributions of the surface pressures are smooth compared to the earlier angular positions. A jump is present at the smallest radius, where the root cavities continue to collapse as the blade begins its ascend.

4.5. Cavitation collapse events and pressure time histories behind the propeller

The behaviour of the pressure fluctuations at the propeller inner and outer radii were studied as follows. The propeller slipstream was divided into two zones in the radial direction by a cylinder of radius $r/R = 0.6$. The upper cylindrical region was located in the axial direction from the propeller trailing edge ($x/D_p = 0.1$) to such a distance downstream that the collapse and rebound of the cavitating tip vortices were captured inside the investigation region. The upper investigation region was limited by a radius $r/R = 1.2$. The lower cylindrical region extended in radial direction from the propeller hub and shaft to the radius $r/R = 0.6$. In the axial direction, the inner investigation region included the volume between the blades and the

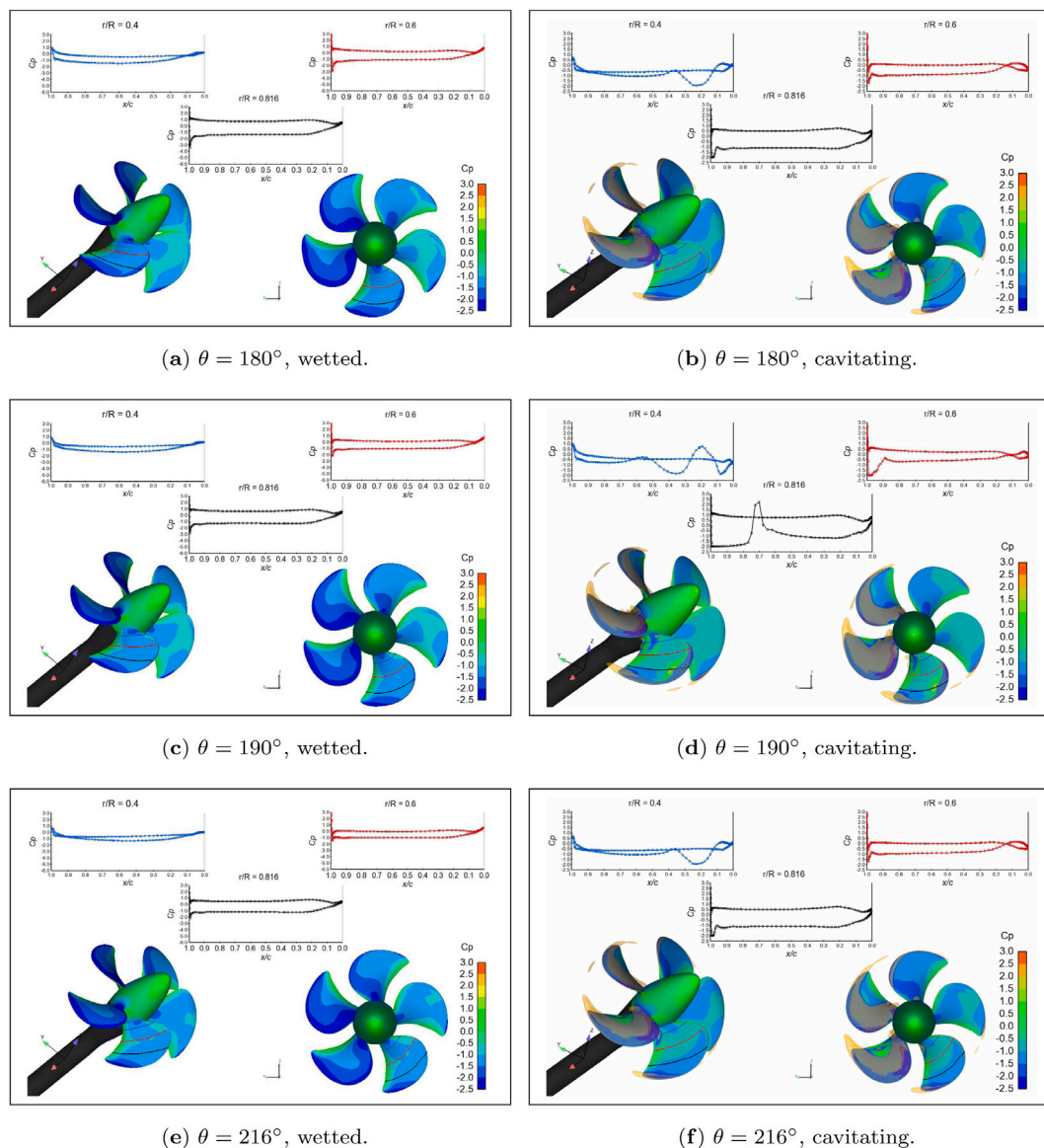


Fig. 21. Pressure distributions at various radii at $\theta = 0^\circ$. The orange transparent region denotes the iso-surface of $\alpha = 0.5$. $J = 1.019$ and $\sigma_n = 2.024$. Note the different scale for the y -axis in the plots for the wetted case. (For interpretation of the references to colour in this figure legend, the reader is referred to the web version of this article.)

region under the upper cylindrical region. We investigated the two regions in an attempt to capture the pressure fluctuation of the collapse of the blade root cavities and the tip vortex cavities separately. Then, the time histories of the maximum values of the pressure coefficient were recorded inside these cylinders. The cylinders are depicted in Fig. 22.

The topmost row of Fig. 23 shows the time history of the maximum pressure coefficient for Case 2.1 conditions in the lower and upper investigation zones, for both the wetted and cavitating conditions. It is seen that the wetted case assumes a rather steady periodic form, with a small amplitude. Usually, the location of the maximum values were either close to the centre radius of the blade, or near the tip vortex region especially when the blades were approaching the bottom-dead-center. The time history of the cavitating conditions shows a completely different behaviour. The signal is highly oscillatory, and the maximum amplitudes reach significantly greater values. At the root region, the location of the maximum pressure coefficient was usually near the junction of the blade and the root, where the strong root cavities collapsed. This always occurred upon the descending of the blade; cf. Figs. 20 and 21. It seems that this type of collapse gave rise

to very large values of the pressure peaks (Fig. 24 below). The upper investigation zone shows the pressure amplitudes associated with the collapsing tip vortex cavitation. The shape of the signal is much more regular, when compared to the time history of the root region. This is due to the more confined area of the time-rate of change of the cavities in this case. The amplitudes of the maximum pressure related to the diminishing tip vortex cavitation are much greater than those of the non-cavitating tip vortex.

The middle row of Fig. 23 shows the time history of the maximum pressure coefficient for Case 2.2 conditions in the lower and upper investigation zones, for both the wetted and cavitating conditions. Again, the wetted case assumes a steady periodic value, with relatively small amplitudes. Also for this case, the usual location for the maximum values of the pressure coefficient were either close to the centre radius of the blade, or near the tip vortex region especially when the blades were approaching the bottom-dead-center. The cavitating conditions show again a rapidly fluctuating signal for the lower and upper investigation zones. The root region is more oscillatory, with again very high maximum amplitudes. The location of the maximum pressure values in the inner cylinder was mainly in the root region, where the cavitation

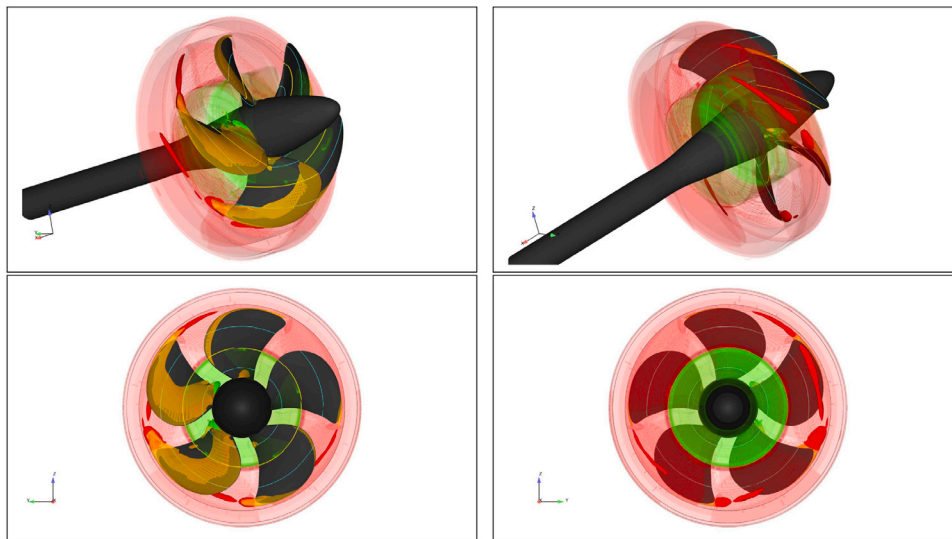
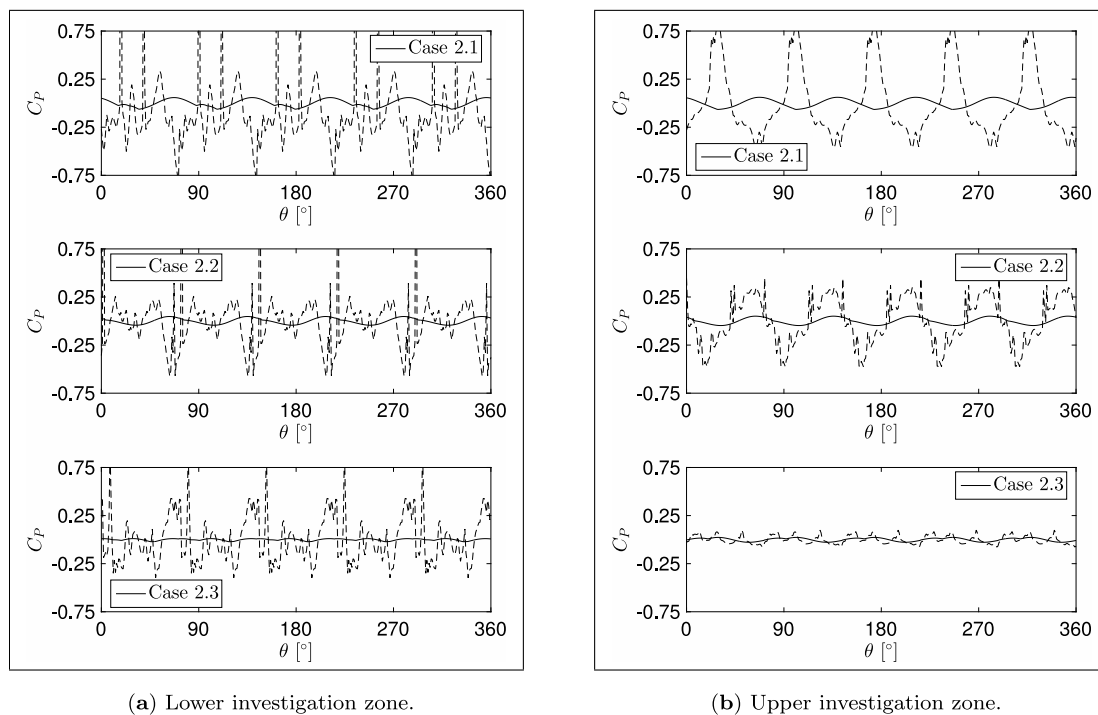


Fig. 22. The location of the two cylindrical investigation zones behind the propeller. The red transparent region denotes the upper investigation zone, and the green transparent region together with the green transparent volumes between the blades denote the lower investigation zone. The red iso-surface denotes the cavitation volume inside the upper investigation zone, and the green iso-surface denotes the cavitation volume inside the lower investigation zone. The orange transparent iso-surface denotes the cavitation in the whole domain. All iso-surfaces are in terms of the volume fraction $\alpha = 0.5$. The yellow circles on the blades denote the radius $r/R = 0.6$. (For interpretation of the references to colour in this figure legend, the reader is referred to the web version of this article.)



(a) Lower investigation zone.

(b) Upper investigation zone.

Fig. 23. The time histories of the maximum pressure coefficient in the two investigation regions. The solid lines correspond to the wetted conditions, and the dashed lines correspond to the cavitating conditions.

was the most severe. Peculiarly, however, the amplitudes of the root cavitation assume lower levels than for the Case 2.1 conditions, despite the fact that the cavitation at the root region appeared harsher in Case 2.2 conditions than in Case 2.1 conditions, cf. Fig. 11. The collapse of the cavitating tip vortex gives rise to higher pressure amplitudes in the upper investigation zone, as would have been expected.

The bottom row of Fig. 23 shows the time history of the maximum pressure coefficient for Case 2.3 conditions in the lower and upper investigation zones, for both the wetted and cavitating conditions. Also for these conditions, the wetted case assumes a steady periodic value, with relatively small amplitudes. Again, the cavitation in the

root region increases the amplitudes of the pressure coefficient in the inner cylinder above those in the wetted conditions. Then again in this case, the predicted cavitating tip vortex was quite mild as we noted in Figs. 11 and 16, which can explain the rather small amplitudes in the upper investigation zone. The pressure amplitudes due to the diminishing cavitating tip vortex are approximately the same as in the non-cavitating conditions.

Lastly, Fig. 24 shows separately the time histories of the wetted and cavitating conditions in both the lower and upper investigation zones. The wetted conditions yield rather smooth and regular distributions in both near the blade root region, and near the blade tip region.

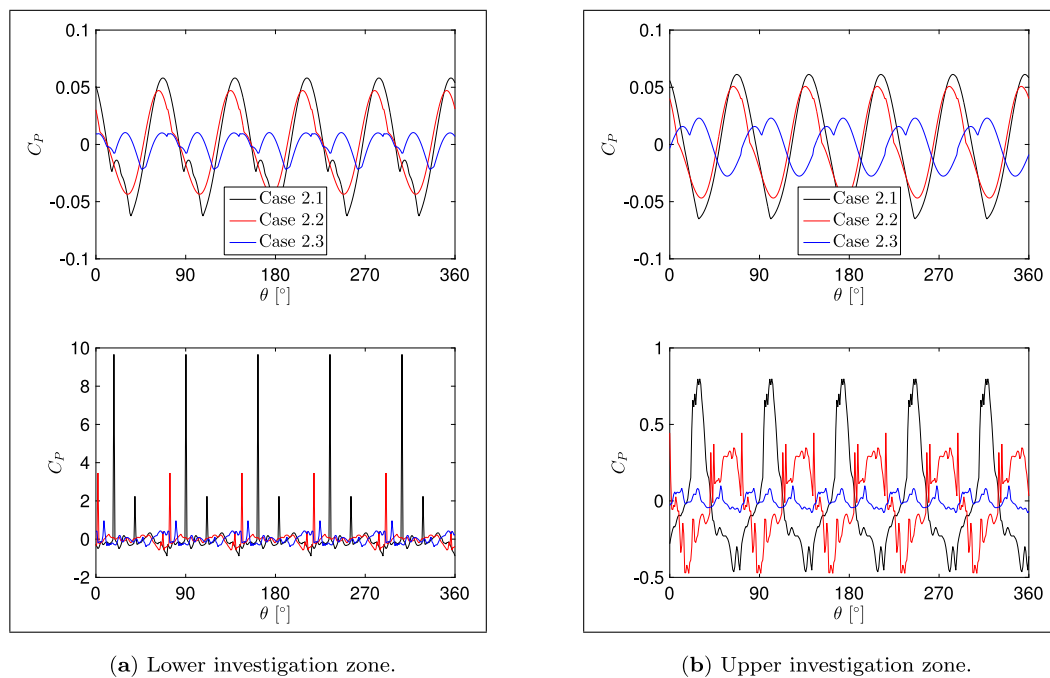


Fig. 24. The time histories of the maximum pressure coefficient in the two investigation regions. The two plots at the top row correspond to the wetted conditions, and the two plots at the bottom row correspond to the cavitating conditions.

Additionally, the amplitudes between the different conditions begin to differ only for Case 2.3. The maximum amplitudes of the pressure coefficient in the root region are very large in the cavitating conditions, the highest peaking at ≈ 10 . This is evident especially for the two highest loading conditions. A very rapid collapse of the unsteady root cavitation was observed to be the cause of the pressure peaks. These collapses occurred close to the junction of the ascending blade and the propeller hub. The maximum amplitudes decrease with the decreasing propeller loading. We observed a similar trend also in the tip region. There, however, the collapse of the cavities is not as violent as in the root region, retaining the peaks at a milder level.

5. Conclusions

In this paper, we analyzed the Potsdam Propeller Test Case studied in the smp'15 Propeller Workshop. The Workshop consisted of three cases, which included the open-water performance curves, cavitation observations as well as pressure pulses induced by the propeller to the ceiling of the cavitation tunnel. The peculiarity of the Workshop was the oblique inflow configuration, establishing a time-dependent problem. The simulations made in accordance with the Workshop cases presented a wide and detailed opportunity to assess the quality of the numerical solutions. The global performance characteristics agreed well with the model test results in both wetted and cavitating conditions. Additionally, the cavitation patterns were predicted reasonably well, given the limitations of the cavitation model. The pressure pulses on the tunnel ceiling were better predicted in the wetted case, which was also noted during the Workshop (Kinnas et al., 2015).

In the oblique flow case, the inflow is not uniform from the perspective of the propeller which results in the dependency of the propeller blade loading and cavitation on the blade rate frequency. The first harmonics were expectedly greater in magnitude than the higher-order components. In the cavitating case, the higher-order terms mostly obtained higher amplitudes than in the wetted cases. The decent agreement between the computed and measured values for the global force coefficients yields a level of confidence for the prediction of the hydrodynamic loads.

The sheet cavitation incepted at an earlier blade position in the simulations than was observed in the tests. The simulations tend to promote the turbulence earlier than the model tests near the leading edge of the blade. In the model tests, the transition from laminar to turbulent flow is delayed on a smooth blade, and consequently the cavitation inception can be delayed. The observed absence of sheet cavitation in the model test is likely caused by laminar flow near the leading edge. Then again, in certain cases the cavitation evolution was very unsteady and complex, consisting of also bubbly regions. Here, the numerical simulations predicted mainly uniform sheet cavitation, or larger cavitation structures. A homogeneous mixture modelling approach on practical grids is not necessarily best suited for detailed prediction of such phenomena. In order to capture the far-wake formation and collapse of the tip vortex and the tip vortex cavitation, a dense grid is required. The entire slipstream of the propeller cannot be filled with an adequate amount of grid points due to limitations in computing power. In a uniform inflow case, the grid points can be concentrated in the regions of the cavitating tip vortex (Viitanen et al., 2020a; Viitanen and Siikonen, 2017; Sipilä et al., 2014) to predict its extension also quite far to the wake, but in an oblique flow case an adaptive grid or more intelligent clustering would be necessary to track the tip vortices in order to keep the total grid size reasonable, since the radial location of the vortex varies more as the propeller rotates. Improving cavitation modelling beyond compressible homogeneous flow models requires more accurate treatment of bubble dynamics or phasic transport phenomena. Bubble dynamics could be coupled with mass-transfer modelling (Muzaferija et al., 2017; Hsiao et al., 2017; Yakubov et al., 2013), or the multiphase media could be more treated with inhomogeneous flow models. An extended model of the latter type is under development by the authors (Viitanen and Peltola, 2021), and we have obtained promising initial results for hydrodynamic cavitation using such an approach.

The unsteady cavitation behind the propeller brought a great increase in the recorded pressure values. The magnitudes grew with the increasing propeller loading. The collapse of the root cavities produced pressure pulses of one order of magnitude larger by their amplitude than the collapsing tip vortex cavitation. Also the collapse of the vapour cavities on the blades of the propeller present a significant increase in

the pressure fluctuations on the blades. These factors in turn can result in an increase in the noise signature generated by the propeller, and the rapid pressure pulses on the blades may cause vibration problems. Additionally, the quickly varying vapour volume close to the surface of the propeller can lead to erosion, especially near the propeller root region.

CRedit authorship contribution statement

Ville Viitanen: Conceptualization, Methodology, Software, Validation, Formal analysis, Resources, Data Curation, Writing – original draft, Writing – review & editing, Visualization. **Tuomas Sipilä:** Conceptualization, Methodology, Software, Validation, Formal analysis, Resources, Writing – review & editing, Supervision, Project administration, Funding acquisition. **Antonio Sánchez-Caja:** Software, Writing – review & editing, Supervision. **Timo Siikonen:** Conceptualization, Methodology, Software, Writing – review & editing, Supervision.

Declaration of competing interest

The authors declare that they have no known competing financial interests or personal relationships that could have appeared to influence the work reported in this paper.

Acknowledgements

V. Viitanen would like to express his gratitude for the support granted by the Finnish Funding Agency for Innovation (TEKES), Finland and the German Federal Ministry for Economic Affairs and Energy within the project “PropNoise”. Without the funding the research project could not have been realized.

References

- Ando, S., Kimura, K., Segawa, K., Yamamoto, K., 2018. Study on the hybrid method of CFD and bubble dynamics for marine propeller cavitation noise prediction. In: CAV2108, Baltimore, USA.
- Asnaghi, A., Feymark, A., Bensow, R., 2017. Improvement of cavitation mass transfer modeling based on local flow properties. *Int. J. Multiph. Flow* 93, 142–157.
- Asnaghi, A., Svennberg, U., Bensow, R., 2018. Analysis of tip vortex inception prediction methods. *Ocean Eng.* 167, 187–203.
- Budich, B., Schmidt, S.J., Adams, N.A., 2015. Numerical investigation of a cavitating model propeller including compressible shock wave dynamics. In: Fourth International Symposium on Marine Propulsors (Smp'15), Austin, Texas, USA.
- Choi, Y.H., Merkle, C.L., 1993. The application of preconditioning in viscous flows. *J. Comput. Phys.* 105, 207–230.
- Eskilsson, C., Bensow, R.E., 2015. Estimation of cavitation erosion intensity using CFD: Numerical comparison of three different methods. In: Fourth International Symposium on Marine Propulsors (Smp'15), Austin, Texas, USA.
- Gaggero, S., Villa, D., 2018. Cavitating propeller performance in inclined shaft conditions with OpenFOAM: PPTC 2015 test case. *J. Mar. Sci. Appl.* 17 (1), 1–20.
- Ge, M., Svennberg, U., Bensow, R., 2020. Investigation on RANS prediction of propeller induced pressure pulses and sheet-tip cavitation interactions in behind hull condition. *Ocean Eng.* 209, 107503.
- Hsiao, C.-T., Ma, J., Chahine, G.L., 2017. Multiscale tow-phase flow modeling of sheet and cloud cavitation. *Int. J. Multiph. Flow.*
- Kinnas, S., Abdel-Maksoud, M., Barkmann, U., Lübke, L., Tian, Y., 2015. Proceedings of the second workshop on cavitation and propeller performance. In: The Fourth International Symposium on Marine Propulsors (smp'15). Workshop: Propeller Performance, Austin, Texas, USA.
- Kunz, R., Boger, D., Stinebring, D., Chyczewski, T., Lindau, J., Gibeling, H., Venkateswaran, S., Govindan, T., 2000. A preconditioned Navier-Stokes method for two-phase flows with application to cavitating prediction. *Comput. Fluids* 29 (8), 849–875.
- Lidtke, A., Humphrey, V., Turnock, S., 2016. Feasibility study into a computational approach for marine propeller noise and cavitation modelling. *Ocean Eng.* 120, 152–159.

- Lloyd, T., Vaz, G., Rijpkema, D., Reverberi, A., 2017. Computational fluid dynamics prediction of marine propeller cavitation including solution verification. In: Fifth International Symposium on Marine Propulsors, Smp'17.
- Martio, J., Sipilä, T., Sánchez-Caja, A., Saisto, I., Siikonen, T., 2011. Evaluation of the propeller hull vortex using a RANS solver. In: Proceedings of the 2nd International Symposium on Marine Propulsors, Hamburg, Germany, Vol. 11.
- Matusiak, J., 2003. Momentum equation applied to the problem of a propeller in oblique flow. *Ship Technol. Res.* 50 (3), 103–105.
- Menter, F.R., 1994. Two-equation eddy-viscosity turbulence models for engineering applications. *AIAA J.* 32 (8), 1598–1605.
- Miettinen, A., 2007. Simple Polynomial Fittings for Steam, CFD/THERMO-55-2007. Report 55, Laboratory of Applied Thermodynamics, Aalto University, Espoo, URL: <http://urn.fi/URN:NBN:fi:aalto-201612135930>.
- Miettinen, A., Siikonen, T., 2015. Application of pressure- and density-based methods for different flow speeds. *Internat. J. Numer. Methods Fluids* 79 (5), 243–267, fld.4051.
- Morgut, M., Jošt, D., Škerlavaj, A., Nobile, E., Contento, G., Pigazzini, R., Puzzer, T., Martini, S., 2019. Numerical simulations of a cavitating propeller in uniform and oblique flow. *Int. Shipbuild. Prog.* 66 (1), 77–90.
- Morgut, M., Nobile, E., Jost, D., Škerlavaj, A., 2015. Numerical predictions of the PPTC model propeller in oblique flow. In: Fourth International Symposium on Marine Propulsors (Smp'15). Workshop: Propeller Performance, Austin, Texas, USA.
- Muzaferija, S., Papoulias, D., Perić, M., 2017. VOF simulations of hydrodynamic cavitation using the asymptotic and classical Rayleigh-pletset models. In: Fifth International Symposium on Marine Propulsors, Espoo, Finland, June. pp. 12–15.
- OpenFOAM, 2016. OpenFOAM. <http://www.openfoam.org/>. Accessed: October 15th, 2016.
- Sakamoto, N., Kamiirisa, H., 2018. Prediction of near field propeller cavitation noise by viscous CFD with semi-empirical approach and its validation in model and full scale. *Ocean Eng.* 168, 41–59.
- Sánchez-Caja, A., González-Adalid, J., Pérez-Sobrino, M., Sipilä, T., 2014. Scale effects on tip loaded propeller performance using a RANSE solver. *Ocean Eng.* 88, 607–617.
- Sánchez-Caja, A., Martio, J., Viitanen, V., Siikonen, T., 2021. Simulation of turbulent effective wakes for propellers in off-design conditions by a correction factor approach. *J. Mar. Sci. Technol.* 26 (4), 1014–1025.
- Sezen, S., Atlar, M., Fitzsimmons, P., Sasaki, N., Tani, G., Yilmaz, N., Aktas, B., 2020. Numerical cavitation noise prediction of a benchmark research vessel propeller. *Ocean Engineering* 211, 107549.
- Singhal, A., Athavale, M., Li, H., Jiang, Y., 2002. Mathematical basis and validation of the full cavitation model. *J. Fluids Eng.* 124.
- Sipilä, T., 2012. RANS Analyses of Cavitating Propeller Flows (Licentiate thesis). Aalto University, School of Engineering, URL: <http://www.vtt.fi/inf/pdf/science/2012/S22.pdf>.
- Sipilä, T., Sánchez-Caja, A., Siikonen, T., 2014. Eddy vorticity in cavitating tip vortices modelled by different turbulence models using the RANS approach. In: 6th European Conference on Computational Fluid Dynamics, (ECFD VI), Vol. Barcelona, Spain.
- Viitanen, V.M., Hynninen, A., Sipilä, T., Siikonen, T., 2018. DDES of wetted and cavitating marine propeller for CHA underwater noise assessment. *J. Mar. Sci. Eng.* 6 (2), 56.
- Viitanen, V., Peltola, J., 2021. Hydrodynamic cavitation investigations with homogeneous and inhomogeneous multiphase flow models in openfoam context. In: 11th International Symposium on Cavitation, Daejeon, Korea. pp. 618–624.
- Viitanen, V., Siikonen, T., 2017. Numerical simulation of cavitating marine propeller flows. In: 9th National Conference on Computational Mechanics (MekIT'17), Trondheim, Norway. URL: http://agricastorres.es/cimnecongress/MEKIT_2017/Ebook%20Mekit17.pdf. International Center for Numerical Methods in Engineering (CIMNE), pp. 385–409. Trondheim, Norway. ISBN: 978-84-947311-1-2.
- Viitanen, V., Siikonen, T., Sánchez-Caja, A., 2020a. Cavitation on model-and full-scale marine propellers: Steady and transient viscous flow simulations at different Reynolds numbers. *J. Mar. Sci. Eng.* 8 (2), 141.
- Wang, Y., Mikkola, T., Hirdaris, S., 2022. A fast and storage-saving method for direct volumetric integration of fwh acoustic analogy. *Ocean Engineering* 261, 112087.
- Yakubov, S., Cankurt, B., Abdel-Maksoud, M., Rung, T., 2013. Hybrid mpi/openmp parallelization of an euler-lagrange approach to cavitation modelling. *Computers & Fluids* 80, 365–371.
- Yilmaz, N., Atlar, M., Fitzsimmons, P., 2018. An improved tip vortex cavitation model for propeller-rudder interaction. In: 10th International Cavitation Symposium (CAV2018).
- Yilmaz, N., Atlar, M., Khorasanchi, M., 2019. An improved mesh adaption and refinement approach to cavitation simulation (MARCS) of propellers. *Ocean Eng.* 171, 139–150.
- Zwart, P., Gerber, A., Belamri, T., 2004. A two-phase model for predicting cavitation dynamics. In: ICMF International Conference on Multiphase Flow, Yokohama, Japan.